Available online at www.sciencedirect.com
SCIENCE DIRECT®
International Journal of Heat and Mass Transfer 47 (2004) 797–808
International Journal of HEAT and MASS TRANSFER
www.elsevier.com/locate/ijhmt

Numerical simulation of natural convection between two elliptical cylinders using DQ method

Y.D. Zhu [a], C. Shu [a,*], J. Qiu [b], J. Tani [b]

[a] Department of Mechanical Engineering, National University of Singapore, 10 Kent Ridge Crescent, 119260, Singapore
[b] Institute of Fluid Science, Tohoku University, Katahira 2-1-1, Aoba-ku, Sendai, Japan

Received 27 November 2002; received in revised form 30 May 2003

Abstract

In this paper, natural convective heat transfer between two horizontal, elliptic cylinders is numerically studied using the differential quadrature (DQ) method. The governing equations are taken to be in the vorticity-stream function formulation. To apply the DQ method, the coordinate transformation is performed. An elliptic function is used, which makes the coordinate transformation from the physical domain to the computational domain be set up by an analytical expression. The present method was validated by comparing its numerical results with available publication data and very good agreement has been achieved. A systematic study is conducted for the analysis of flow and thermal fields at different eccentricities and angular positions. It was found that the position of the major axis of the inner ellipse takes effect on the streamlines, and very little effect on the average Nusselt number.

Keywords: Natural convection; DQ; Elliptical cylinders; N–S equations; Incompressible

1. Introduction

Flow and heat transfer in an annulus are of practical importance in engineering applications and involved in many industrial systems. Applications of natural convection include solar collector receivers, transmission cable cooling systems, food processing, cooling of electronic equipment, aircraft cabin insulation, cooling system in nuclear reactor and etc. In the past a few decades, natural convection in the case of a horizontal circular annulus was widely studied experimentally and numerically. The work of Kuehn and Goldstein [1] can be referred as a comprehensive review for concentric cases. The experimental and analytical studies for the eccentric cases include the work of Kuehn and Goldstein [2], Guj and Stella [3].

Comparatively, fewer publications were found for natural convection in a non-circular domain, e.g., the elliptic domain considered in this paper. Lee and Lee [4] attempted to simulate the natural convection problem in terms of elliptical coordinates for the symmetrical cases of elliptical annuli and performed experiments for this geometry with a few cases. Schreiber and Singh [5] studied the cases in horizontal confocal elliptical cylinders oriented at an arbitrary angle with respect to the gravity vector in the same coordinate system. Cheng and Chao [6] employed the body-fitted coordinate transformation method to generate a non-staggered curvilinear coordinate system and performed numerical study for some horizontal eccentric elliptical annuli. Elshamy et al. [7] studied numerically the case in horizontal confocal elliptical annulus and developed some practical correlations for the average Nusselt number. Publications in this field are very few, and there is much work to do for further investigation.

In the numerical simulation of natural convection, low order methods such as finite difference, finite volume and finite element methods were usually used. For

* Corresponding author. Tel.: +65-6874-6476; fax: +65-6779-1459.
E-mail address: mpeshuc@nus.edu.sg (C. Shu).

0017-9310/$ - see front matter © 2003 Elsevier Ltd. All rights reserved.
doi:10.1016/j.ijheatmasstransfer.2003.06.005

example, the work of Kuehn and Goldstein [1] and Stella and Guj [8] was conducted by the finite difference method, and the work of Schreiber and Singh [5] and Cheng and Chao [6] was made respectively by the finite element and finite volume method. In general, the low order methods need a large number of grid points to obtain accurate numerical results, and as a consequence, require large computational effort and virtual storage. To save the computational effort, and in the meantime, to obtain accurate numerical results, some efficient methods are demanded. The differential quadrature (DQ) method [9,10] is such an efficient method, which approximates the derivative of a function at any location by a linear summation of all the functional values along a mesh line. It can obtain very accurate numerical results by using a considerably small number of grid points and requires very little computational effort. So far, the DQ method has been widely applied in engineering [11–15]. However, most of its applications are limited to simple physical domains. Like the conventional low order finite difference schemes, the DQ method also requires the computational domain to be regular. For irregular domain problems such as the one considered in this study, the coordinate transformation technique should be introduced. In this technique, the irregular physical domain is first transformed into a regular computational domain, and the governing equations as well as the boundary conditions are transformed into the relevant forms in the computational space. Then all the computations including the discretization of derivatives by the DQ method are based on the computational space. Using this technique, Shu et al. [16] efficiently simulate the natural convection in an annulus between two eccentric circular cylinders by using the DQ method. They presented an explicit formulation to compute the stream function value on the inner cylinder wall, which can efficiently capture the weak global circulation. It was also found in [16] that the configuration of annulus has a great effect on the flow and thermal fields. The present work was motivated from further study of annulus configuration effect on the flow and thermal fields, and further exploration for the performance of DQ method to irregular domain problems.

In the study, numerical analysis for natural convection between two horizontal concentric elliptic cylinders is performed to evaluate the heat transfer characteristics and flow patterns under various geometrical and physical conditions. Eccentricity between the outer and the inner elliptic cylinders is not considered in this study, as the different eccentricities of both the outer and inner cylinders yield too many sets of geometrical combinations. The vorticity-stream function formulation is taken as the governing equation, and the elliptic function is used for approximating the elliptic boundary. As a result, the coordinate transformation from the physical domain to the computational domain is set up by an analytical expression. The SOR iteration method is applied to solve the resultant algebraic equations. A systematic study is conducted for the analysis of flow and thermal fields at different elliptic eccentricities and angular positions.

2. The DQ method

The DQ method is a numerical discretization technique for approximation of derivatives. It was proposed by Bellman and his associates in the early of 1970s [9]. In their work, a partial derivative of a function with respect to a coordinate direction is expressed as a linear weighted sum of all the functional values at all grid points along that direction. The key to the DQ method is the determination of the weighting coefficients for any order derivative approximation. A major breakthrough was made by Shu and his colleagues [11,12], in development of explicit formulations for computing the weighting coefficients. For brevity, a one-dimensional problem is chosen in the following to demonstrate the DQ method, where the first- and second-order derivatives of $f(x)$ at a point x_i are approximated by

$$f_x(x_i) = \sum_{j=1}^{N} a_{ij} \cdot f(x_j) \quad \text{for } i = 1, 2, \ldots, N \tag{1}$$

$$f_{xx}(x_i) = \sum_{j=1}^{N} b_{ij} \cdot f(x_j) \quad \text{for } i = 1, 2, \ldots, N \tag{2}$$

where N is the number of grid points, a_{ij} and b_{ij} are respectively the first- and second-order weighting coefficients. It was shown by Shu and Richards [11] and Shu and Xue [12] that all the ways of computing the weighting coefficients can be generalized under the analyses of function approximation and linear vector space. It was found that when the function $f(x)$ is approximated differently, the formulations for a_{ij} and b_{ij} are also different. In the following, the respective formulations of a_{ij} and b_{ij} are presented when the function $f(x)$ is approximated by a high order polynomial or by the Fourier series expansion.

3. Polynomial-based differential quadrature

In this case, it is supposed that the function is approximated by a $(N-1)$th degree polynomial in the form

$$f(x) = \sum_{k=0}^{N-1} c_k \cdot x^k \tag{3}$$

Under the analysis of a linear vector space, Shu and Richards [11] derived the following explicit formulations to compute the weighting coefficients:

$$a_{ij} = \frac{M^{(1)}(x_i)}{(x_i - x_j)\cdot M^{(1)}(x_j)}, \quad \text{when } j \neq i \tag{4a}$$

$$a_{ii} = -\sum_{k=1,k\neq i}^{N} a_{ik} \tag{4b}$$

$$b_{ij} = 2a_{ij}\cdot\left(a_{ii} - \frac{1}{x_i - x_j}\right), \quad \text{when } j \neq i \tag{5a}$$

$$b_{ii} = -\sum_{k=1,k\neq i}^{N} b_{ik} \tag{5b}$$

where

$$M^{(1)}(x_i) = \prod_{k=1,k\neq i}^{N} (x_i - x_k)$$

It is indicated that a recurrence relationship has also been derived to compute the weighting coefficients of the higher order derivatives. For details, see the book of Shu [10].

4. Fourier expansion-based differential quadrature

In this case, the function is approximated by a Fourier series expansion in the form

$$f(x) = c_0 + \sum_{k=1}^{N/2}(c_k \cos kx + d_k \sin kx) \tag{6}$$

Similar to polynomial-based differential quadrature (PDQ), Shu and Xue [12] also derived the explicit formulations to compute the weighting coefficients a_{ij} and b_{ij}, which are listed below

$$a_{ij} = \frac{1}{2}\cdot\frac{P(x_i)}{\sin\frac{x_i - x_j}{2}\cdot P(x_j)}, \quad \text{when } j \neq i \tag{7a}$$

$$a_{ii} = -\sum_{k=1,k\neq i}^{N} a_{ik} \tag{7b}$$

$$b_{ij} = a_{ij}\left[2a_{ii} - \cot\frac{x_i - x_j}{2}\right], \quad \text{when } j \neq i \tag{8a}$$

$$b_{ii} = -\sum_{k=1,k\neq i}^{N} b_{ik} \tag{8b}$$

where

$$P(x_i) = \prod_{k=0,k\neq i}^{N} \sin\frac{x_i - x_k}{2}$$

It should be indicated that Eqs. (7) and (8) can be applied to the periodic problems and the non-periodic problems. For the non-periodic problems, the x range in the computational domain is $0 \leqslant x \leqslant \pi$, while for the periodic problems, the x range in the computational domain is $0 \leqslant x < 2\pi$. For details, see the work of Shu and Xue [12].

DQ is a global method. Its major advantage is that it can obtain very accurate numerical results by using a considerably small number of mesh points. As shown in [15], for a Poisson problem, the DQ method with the mesh size of 11×11 can achieve the same order of accuracy as the second-order FD scheme with the mesh size of 75×75. Since much less number of mesh points is used in the DQ method, it requires much less computational effort and virtual storage. Both the PDQ and Fourier expansion-based differential quadrature (FDQ) methods can be applied to the periodic and non-periodic problems. However, it was demonstrated in the book of Shu [10] that PDQ method has a better performance than the FDQ method for a non-periodic condition, while the FDQ method has a better performance than the PDQ method for the periodic condition since the periodic condition is inherently built in the FDQ formulation. So, in this work, the derivatives in the radial direction are discretized by the PDQ method while the derivatives in the circumferential direction are discretized by the FDQ method.

5. Governing equations and boundary conditions

In this study, heat is generated uniformly within the inner cylinder, while the outer cylinder is concentrated with the inner cylinder and is cold. The imposed boundary conditions are no-slip and isothermal on both cylinder walls. As the cylinders are long enough, the flow is considered to be two-dimensional. It is also assumed that the flow is steady and laminar. The buoyancy force is the driven force for the flow.

Based on the Boussinesq approximation, the non-dimensional governing equation for the problem is written in the vorticity-stream function formulation as

$$\frac{\partial^2\psi}{\partial x^2} + \frac{\partial^2\psi}{\partial y^2} = \omega \tag{9}$$

$$u\frac{\partial\omega}{\partial x} + v\frac{\partial\omega}{\partial y} = Pr\left(\frac{\partial^2\omega}{\partial x^2} + \frac{\partial^2\omega}{\partial y^2}\right) - PrRa\frac{\partial T}{\partial x} \tag{10}$$

$$u\frac{\partial T}{\partial x} + v\frac{\partial T}{\partial y} = \frac{\partial^2 T}{\partial x^2} + \frac{\partial^2 T}{\partial y^2} \tag{11}$$

where ψ denotes stream function, ω represents vorticity, T is temperature. Prandtl number is defined as $Pr = \mu C_p/k$, Rayleigh number is defined as $Ra = C_p\rho_0 g\beta L^3\Delta T/(k\nu)$. Here μ is viscosity, C_p is specific heat at constant pressure, k is thermal conductivity, ρ_0 is reference density, g is gravitational acceleration, β is thermal expansion coefficient, L is the reference length, ΔT is the temperature difference between inner and outer

cylinders, v is kinematic viscosity. Velocity components u and v can be computed from the stream function ψ as

$$u = \frac{\partial \psi}{\partial y}, \quad v = -\frac{\partial \psi}{\partial x} \tag{12}$$

The vorticity ω is defined and computed by

$$\omega = \frac{\partial u}{\partial y} - \frac{\partial v}{\partial x} \tag{13}$$

Like the low order finite difference schemes, the DQ method requires the physical boundary to be a mesh line. In the present study, however, the physical boundaries may not coincide with the mesh lines. When the DQ method is applied to this case, the physical boundary conditions cannot be implemented in a straightforward way. To overcome this difficulty, the following transformation from the physical space to the computational space is required:

$$\begin{cases} \xi = \xi(x, y) \\ \eta = \eta(x, y) \end{cases} \tag{14}$$

With this transformation, the governing equations (9)–(11) can be transformed to the following forms in the computational space:

$$A\frac{\partial^2 \psi}{\partial \xi^2} + 2B\frac{\partial^2 \psi}{\partial \eta \partial \xi} + C\frac{\partial^2 \psi}{\partial \eta^2} + G\frac{\partial \psi}{\partial \eta} + H\frac{\partial \psi}{\partial \xi} = J\omega \tag{15}$$

$$U\frac{\partial \omega}{\partial \xi} + V\frac{\partial \omega}{\partial \eta} = Pr\left(A\frac{\partial^2 \omega}{\partial \xi^2} + 2B\frac{\partial^2 \omega}{\partial \xi \partial \eta} + C\frac{\partial^2 \omega}{\partial \eta^2} + G\frac{\partial \omega}{\partial \eta} + H\frac{\partial \omega}{\partial \xi}\right) - PrRa\left(y_\eta \frac{\partial T}{\partial \xi} - y_\xi \frac{\partial T}{\partial \eta}\right) \tag{16}$$

$$U\frac{\partial T}{\partial \xi} + V\frac{\partial T}{\partial \eta} = \left(A\frac{\partial^2 T}{\partial \xi^2} + 2B\frac{\partial^2 T}{\partial \xi \partial \eta} + C\frac{\partial^2 T}{\partial \eta^2} + G\frac{\partial T}{\partial \eta} + H\frac{\partial T}{\partial \xi}\right) \tag{17}$$

where

$$U = \frac{\partial \psi}{\partial \eta}, \quad V = -\frac{\partial \psi}{\partial \xi} \quad A = \alpha/J, \quad B = -\sigma/J$$

$$C = \gamma/J, \quad G = \frac{\partial B}{\partial \xi} + \frac{\partial C}{\partial \eta} \quad H = \frac{\partial A}{\partial \xi} + \frac{\partial D}{\partial \eta},$$

$$\alpha = x_\eta^2 + y_\eta^2, \quad \sigma = x_\xi x_\eta + y_\xi y_\eta, \quad \gamma = x_\xi^2 + y_\xi^2,$$

$$J = x_\xi y_\eta - y_\xi x_\eta$$

x_ξ, x_η, y_ξ and y_η are respectively the abbreviations of $\partial x/\partial \xi$, $\partial x/\partial \eta$, $\partial y/\partial \xi$ and $\partial y/\partial \eta$.

As the global circulation flow along the inner cylinder does not exist, stream function values on the inner and outer cylinders are set to zero. From the no-slip condition, the velocities U and V on both the inner and outer cylinder walls are zero. As shown in Fig. 1, the boundary conditions for the problem can be taken as

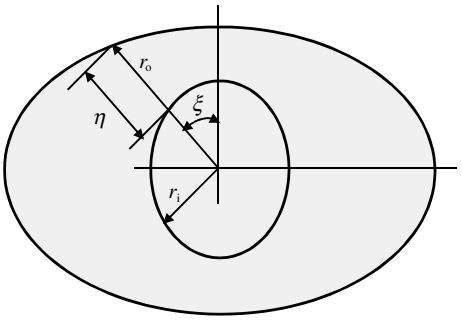

Fig. 1. A schematic view of physical domain.

$$U|_{\eta=0,1} = 0, \quad V|_{\eta=0,1} = 0 \tag{18}$$

$$\psi|_{\eta=0} = 0, \quad \psi|_{\eta=1} = 0 \tag{19}$$

$$T|_{\eta=0} = 1, \quad T|_{\eta=1} = 0 \tag{20}$$

$$\omega|_{\eta=0,1} = \frac{C}{J}\frac{\partial^2 \psi}{\partial \eta^2}\bigg|_{\eta=0,1} = \frac{C}{J}\frac{\partial U}{\partial \eta}\bigg|_{\eta=0,1} \tag{21}$$

$$\frac{\partial \psi}{\partial \eta}\bigg|_{\eta=0,1} = 0 \tag{22}$$

In the ξ direction, the periodic condition is used, which is automatically implemented by the FDQ method.

6. Geometric relationship and analytical coordinate transformation

A schematic view of a horizontal concentric annulus between two elliptic cylinders is shown in Fig. 1. Nine configurations of annulus between two elliptic cylinders are shown in Fig. 2, where the circle is taken as a special case of ellipse. For each ellipse, four elliptic eccentricities, i.e., $\varepsilon = 0.25$, 0.50, 0.75 and 0.95, are taken into consideration. It should be noted that the elliptic eccentricity here is the elliptic eccentricity of the ellipse itself, not the eccentricity of the location of the outer cylinder to the inner cylinder. The geometric relationships of the physical domains will be shown in the following.

The physical domain is formed between two concentric elliptic cylinders. For a single ellipse, it can be represented by its eccentricity. Setting a as the major axis and b as the minor axis, the eccentricity is defined as

$$\varepsilon = \sqrt{a^2 - b^2}/a \tag{23}$$

Defining γ as the ratio of the minor axis length over the major axis length of an ellipse,

$$\gamma_{ba} = b/a \tag{24}$$

we have the following relationships:

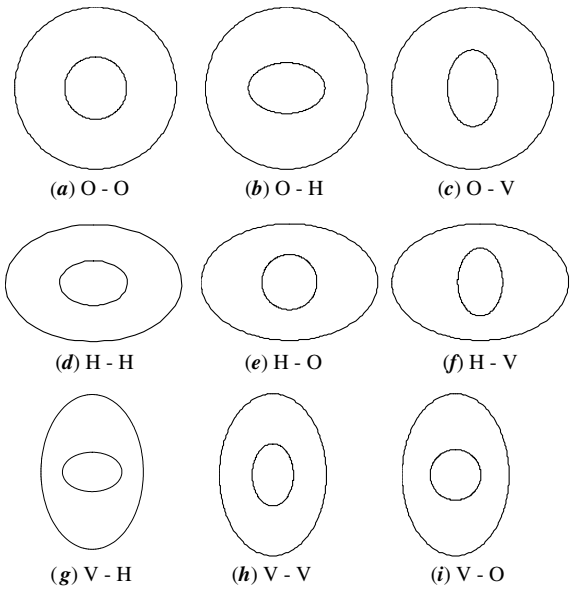

Fig. 2. Nine configurations of an annulus between two elliptic cylinders. Here "H" in the "H–V" configuration represents the orientation of major axis of the outer ellipse which is placed horizontally, "V" shows the orientation of major axis of the inner ellipse which is placed vertically. Other configurations have similar definitions. "O" represents a circle.

$$\gamma_{ba} = \sqrt{1-\varepsilon^2} \tag{25}$$

$$b = \sqrt{1-\varepsilon^2}\cdot a \tag{26}$$

The geometric relationship between the inner and the outer elliptic cylinders can be represented by the aspect ratio, which is fixed in this study, and the orientation as well, i.e., the major axis of an ellipse is placed either horizontally or vertically. Setting the aspect ratio as

$$rr = \bar{r}_o/\bar{r}_i \tag{27}$$

where $\bar{r}_o$ denotes the radius of a circle with equivalent area to the outer ellipse, $\bar{r}_i$ the radius of a circle with equivalent area to the inner ellipse. Since the area of an ellipse is πab, we have

$$\bar{r}_o = \sqrt{a_o b_o} \tag{28a}$$

$$\bar{r}_i = \sqrt{a_i b_i} \tag{28b}$$

where the subscripts o and i represent the outer and inner ellipses respectively.

Using Eqs. (26) and (28), the axes of an ellipse can be expressed in the following:

$$a_o = \frac{\bar{r}_o}{(1-\varepsilon_o^2)^{1/4}}, \quad b_o = (1-\varepsilon_o^2)^{1/4}\cdot\bar{r}_o \tag{29a}$$

$$a_i = \frac{\bar{r}_i}{(1-\varepsilon_i^2)^{1/4}}, \quad b_i = (1-\varepsilon_i^2)^{1/4}\cdot\bar{r}_i \tag{29b}$$

Defining the length scale L as

$$L = \bar{r}_o - \bar{r}_i \tag{30}$$

we have the following formula for calculating the axes of an ellipse:

$$\frac{a_o}{L} = \frac{1}{(1-\varepsilon_o^2)^{1/4}}\cdot\frac{rr}{rr-1} \tag{31a}$$

$$\frac{b_o}{L} = (1-\varepsilon_o^2)^{1/4}\cdot\frac{rr}{rr-1} \tag{31b}$$

$$\frac{a_i}{L} = \frac{1}{(1-\varepsilon_i^2)^{1/4}}\cdot\frac{1}{rr-1} \tag{32a}$$

$$\frac{b_i}{L} = (1-\varepsilon_i^2)^{1/4}\cdot\frac{1}{rr-1} \tag{32b}$$

With above relationships, the coordinate transformation from the physical space to the computational space can be exactly set up. The elliptic function for the concentric elliptic cylinder can be written as

$$\left(\frac{x}{a}\right)^2 + \left(\frac{y}{b}\right)^2 = 1 \tag{33}$$

With Eq. (33), the coordinate transformation for the present problem is set up as

$$x = -\sin\xi\cdot[r_i + (r_o - r_i)\eta] \tag{34a}$$

$$y = \cos\xi\cdot[r_i + (r_o - r_i)\eta] \tag{34b}$$

where r_i and r_o are derived from Eq. (33) as

$$r_o = \frac{b_o}{\left[\left(\frac{b_o}{a_o}\right)^2(\sin\xi)^2 + (\cos\xi)^2\right]^{\frac{1}{2}}} \tag{35a}$$

$$r_i = \frac{b_i}{\left[\left(\frac{b_i}{a_i}\right)^2(\sin\xi)^2 + (\cos\xi)^2\right]^{\frac{1}{2}}} \tag{35b}$$

The transformed computational domain in the (ξ,η) plane is $0\leqslant\eta\leqslant 1$ and $0\leqslant\xi\leqslant\pi$.

7. Results and discussion

In the present study, Rayleigh number is fixed at 10^4 in a steady laminar flow regime. Air is considered to be the working fluid and Prandtl number is set to be 0.71. The aspect ratio of the outer cylinder over the inner cylinder is fixed at 2.6. Vertical and horizontal orientations are taken for either the outer or the inner cylinder. Four elliptic eccentricities, i.e., 0.25, 0.50, 0.75 and 0.95, are taken into consideration for each case. The PDQ method is applied in the η direction with non-uniform grid point distribution, while the FDQ method is applied in the ξ direction with uniform grid point distribution. The grid point distributions are taken as

$$\xi_i = \frac{i-1}{N}\cdot 2\pi, \quad i = 1,2,\ldots,N \tag{36a}$$

$$\eta_j = \frac{1}{2}\left[1-\cos\left(\frac{j-1}{M-1}\pi\right)\right], \quad j = 1,2,\ldots,M \tag{36b}$$

After numerical discretization by the DQ method, the resultant algebraic equations are solved by the SOR iteration method. The convergence criteria are chosen as $|R_\psi|_{\max} \leqslant 10^{-4}$, $|R_T|_{\max} \leqslant 10^{-4}$ and $|R_\omega|_{\max} \leqslant 10^{-2}$ for ψ, T and ω equations respectively, where $|R_\psi|_{\max}$, $|R_T|_{\max}$ and $|R_\omega|_{\max}$ are the maximum absolute residual values for the stream function, temperature and vorticity equations respectively. When all the three criteria are satisfied, the convergent results are subsequently obtained. In the present study, the initial values are set to zero for all ψ, u, v, T and ω at interior points.

7.1. Grid independent study

The grid-independent study is performed for the case of $Ra = 10^4$, $rr = 2.6$, $Pr = 0.71$, $\varepsilon_o = 0.50$, $\varepsilon_i = 0.50$, and both outer and inner ellipses are in horizontal positions. The results are shown in Table 1. It is shown that when mesh size is above 31×17, the computed $\psi_{\max}$ and $\overline{Nu}$ remain the same for this case. It should be noted that the minimum mesh size for accurate numerical solution changes according to the eccentricity of the ellipse and the orientation of the physical domains. In this study, mesh sizes of 31×21, 51×31, 61×31, 71×31 as well as 71×41 are taken for different cases, based on the eccentricities and the orientations of both cylinders.

Table 1
Grid-independent study ($Ra = 10^4$, $rr = 2.6$, $Pr = 0.71$, $\varepsilon_o = 0.50$, $\varepsilon_i = 0.50$)

No.	Orientation	Grid size	$\psi_{\max}$	$\overline{Nu}$
1	H–H	17×13	13.97	3.26
2		21×15	13.18	3.25
3		31×17	13.20	3.25
4		31×21	13.20	3.25
5		41×21	13.20	3.25
6		51×21	13.20	3.25
7		51×31	13.20	3.25

7.2. Definition of Nusselt number

The local Nusselt number in the physical domain is defined as

$$Nu = -\frac{\partial T}{\partial n} \tag{37}$$

where $\partial/\partial n$ is the normal derivative outward from the surface. In the computational domain, it becomes

$$Nu = \frac{1}{J\sqrt{\gamma}}\left(\beta\frac{\partial T}{\partial \xi} - \gamma\frac{\partial T}{\partial \eta}\right) \tag{38}$$

where J, β and γ are defined previously. The average Nusselt number is obtained by integrating the local Nusselt numbers around the inner cylinder wall.

7.3. Validation of numerical results

As discussed in Section 1, publications are very few on the study of natural convection in annuli between concentric elliptic cylinders. The work of Elshamy et al. [7] is one of such studies. Elshamy et al. [7] studied numerically natural heat transfer for air bounded by two confocal horizontal elliptic cylinders. The local and average Nusselt numbers are determined for Rayleigh numbers from 10^4 to 2×10^5 at some eccentricities of the inner elliptic cylinder. Their numerical data were validated by comparison with some experimental data and found in a good agreement. Thus, in this study, the results of Elshamy et al. [7] are used to validate the present numerical results. The average Nusselt number $\overline{Nu}$ between the present work and the work of Elshamy et al. [7] are compared in Table 2 for six cases. It should be noted that due to the different ways of non-dimensionalization between the work of Elshamy et al. [7] and the present study, the equivalent factor has to be considered in comparison of the average Nusselt numbers. In the work of Elshamy et al. [7], the reference length for Nusselt number is taken as the difference of the minor axis lengths between the outer and inner elliptic cylinders, while in present study, the reference length is taken as the gap L, defined in Eq. (30). The factor is proportional to the ratio of these two different reference lengths

Table 2
Validation of numerical results

No.	ε_o	ε_i	Orientation	Ra	$\overline{Nu}$ (equivalent)	
					Elshamy et al. [7]	Present
1	0.688	0.4	Vertical	10^4	2.66	2.62
2	0.86	0.4	Vertical	10^4	3.68	3.58
3	0.86	0.4	Vertical	4×10^4	5.34	5.18
4	0.9	0.4	Horizontal	10^4	2.51	2.71
5	0.9	0.4	Horizontal	6×10^4	4.17	4.11
6	0.9	0.4	Horizontal	2×10^5	5.56	5.32

for the average Nusselt numbers. Taking note that the average Nusselt numbers from Elshamy et al. [7] in Table 2 are the equivalent ones after taking into consideration of the equivalent factors, it can be seen that the present results generally agree well with those of Elshamy et al. [7].

7.4. Analysis of flow and thermal fields

With the confidence of validation as well as grid independent study, the flow and thermal fields for nine configurations of annuli as shown in Fig. 2 are numerically analyzed. A sum of 68 different physical domains is considered, which are based on the combination of orientation and eccentricity of the two elliptic cylinders. The values of ψ_{max} and $\overline{Nu}$ for these 68 cases are listed in Tables 3–6, where the configuration denotes the position of major axis of the ellipses. For example, "O–H" means that the outer ellipse is a circle and the major axis of the inner ellipse is in the horizontal direction. "V–O" indicates that the major axis of the outer ellipse is in the vertical direction and the inner ellipse is a circle. "H–V" denotes that the major axes of the outer and inner ellipses are respectively in the horizontal and vertical directions.

The typical streamlines and isotherms are shown in Figs. 3–10. For the streamlines, it is observed that the flow is generally symmetrical about the vertical centerline through the center of the inner elliptic cylinder. It moves up along the inner heated elliptic cylinder. When the flow reaches the top of the outer elliptic cylinder, it then moves horizontally outwards and goes down along the boundary of the outer elliptic cylinder. The details are discussed below.

Table 3
Numerical results for "O–O", "O–H", "O–V", "H–O", "V–O" configurations ($rr = 2.6$, $Ra = 10^4$)

No.	Configuration	ε_o	ε_i	ψ_{max}	$\overline{Nu}_i$
1	O–O	0	0	13.02	3.32
2	O–H	0	0.25	12.92	3.31
3			0.50	12.58	3.28
4			0.75	12.00	3.16
5			0.95	12.90	2.65
6	O–V	0	0.25	13.12	3.32
7			0.50	13.45	3.34
8			0.75	14.18	3.32
9			0.95	15.66	3.02
10	H–O	0.25	0	13.17	3.31
11		0.50		13.63	3.29
12		0.75		13.31	3.50
13		0.95		11.22	3.76
14	V–O	0.25	0	12.88	3.32
15		0.50		12.56	3.34
16		0.75		13.48	3.30

Table 4
Numerical results for "H–H" configuration ($rr = 2.6$, $Ra = 10^4$)

No.	Configuration	ε_o	ε_i	ψ_{max}	$\overline{Nu}_i$
1	H–H	0.25	0.25	13.07	3.30
2			0.50	12.70	3.27
3			0.75	11.94	3.15
4			0.95	12.68	2.63
5		0.50	0.25	13.54	3.28
6			0.50	13.20	3.25
7			0.75	12.24	3.13
8			0.95	11.70	2.60
9		0.75	0.25	13.24	3.50
10			0.50	12.97	3.50
11			0.75	13.23	3.06
12			0.95	9.70	2.55
13		0.95	0.25	11.20	3.72
14			0.50	11.13	3.60
15			0.75	10.94	3.33
16			0.95	10.17	2.74

Table 5
Numerical results for "H–V" configuration ($rr = 2.6$, $Ra = 10^4$)

No.	Configuration	ε_o	ε_i	ψ_{max}	$\overline{Nu}_i$
1	H–V	0.25	0.25	13.27	3.32
2			0.50	13.59	3.33
3			0.75	14.29	3.31
4			0.95	15.70	3.03
5		0.50	0.25	13.71	3.29
6			0.50	14.00	3.30
7			0.75	14.56	3.28
8			0.95	15.76	3.09
9		0.75	0.25	13.39	3.49
10			0.50	13.65	3.46
11			0.75	14.35	3.31
12			0.95	15.23	3.46
13		0.95	0.25	11.24	3.80
14			0.50	11.30	3.96
15			0.75	11.45	4.55
16			0.88	11.62	34.41

The "O–O" configuration is actually the annulus between two circular cylinders. This case has been well studied by many researchers such as Shu et al. [16]. The present results of the maximum stream function value and the average Nusselt number agree very well with those of Shu et al. [16].

For the "O–H" configuration, when ε_i increases from 0 to 0.75, two vortices exist in the streamlines above the centre of the inner cylinder, and move to the top of the physical domain. The maximum stream function value

Table 6
Numerical results for "V–H" and "V–V" configurations ($rr = 2.6$, $Ra = 10^4$)

No.	Configuration	ε_o	ε_i	ψ_{max}	$\overline{Nu}_i$
1	V–H	0.25	0.25	12.78	3.31
2			0.50	12.48	3.28
3			0.75	12.13	3.16
4			0.95	13.10	2.67
5		0.50	0.25	12.53	3.33
6			0.50	12.51	3.30
7			0.75	12.86	3.16
8			0.95	13.66	2.78
9	V–V	0.25	0.25	12.97	3.33
10			0.50	13.30	3.34
11			0.75	14.05	3.33
12			0.95	15.60	3.00
13		0.50	0.25	12.60	3.34
14			0.50	12.80	3.36
15			0.75	13.50	3.35
16			0.95	15.38	3.00
17		0.75	0.25	13.41	3.31
18			0.50	13.17	3.35
19			0.75	12.55	3.37
20			0.95	13.96	3.05

decreases from 13.02 to 12.00, and then increases to 12.90 when ε_i increases to 0.95, as shown in Table 3. Two additional vortices appear below the inner cylinder at $\varepsilon_i = 0.95$ due to the enlarged space below the inner cylinder. This results in a slightly higher maximum stream function value. When ε_i increases from 0.25 to 0.95, the gradient of temperature around the inner cylinder gets smaller, and the average Nusselt number decreases gradually from 3.32 to 2.65. The typical streamlines and isotherms for the case of $\varepsilon_o = 0$, $\varepsilon_i = 0.95$ are shown in Fig. 3, where four vortices can be seen clearly.

For the "O–V" configuration, two vortices in the streamlines locate beside the inner cylinder, and no additional vortex appears. When ε_i increases from 0.25 to 0.95, the inner cylinder occupies less space in the horizontal direction, thus the buoyancy force takes more effect, and the maximum stream function value increases gradually from 13.12 to 15.66, as indicated in Table 3. For $\varepsilon_i = 0.25$, 0.50 and 0.75, one plume appears above the inner cylinder in the isotherms, and the average Nusselt number keeps almost the same. Then it decreases from 3.32 to 3.02 when ε_i increases from 0.75 to 0.95, as two plumes appear above the inner cylinder in the isotherms. The typical streamlines and isotherms for the case of $\varepsilon_o = 0$, $\varepsilon_i = 0.95$ are shown in Fig. 4, where the two plumes can be seen clearly.

For the "H–O" configuration, when ε_o increases from 0.25 to 0.95, the maximum stream function value changes irregularly, and so does the average Nusselt number. It is indicated in Table 3 that the maximum stream function value increases from 13.17 to 13.63 when ε_o increases from 0.25 to 0.50. Two vortices exist beside the inner circular cylinder. Two additional vortices appear above the inner cylinder at $\varepsilon_o = 0.75$ when the space above the inner cylinder reduces to a certain amount. As two additional vortices locate on top of the inner cylinder, they reduce the strength of the stream function, which results in a slightly smaller stream function value. When ε_o increases further to 0.95, it decreases further to 11.22 due to a larger horizontal gap between the two cylinders in the physical domain. When ε_o increases from 0.25 to 0.50, the only plume gets wider above the inner cylinder in the isotherms, and $\overline{Nu}$ reduces slightly from 3.31 to 3.29. At $\varepsilon_o = 0.75$ and 0.95, two plumes plus one additional one in a reverse direction come out when the space above the top of the inner cylinder reduces to an appropriate level, where the additional plume in the reverse direction produces thermal boundary layer to the inner cylinder. The average Nusselt number then increases gradually with the increase of

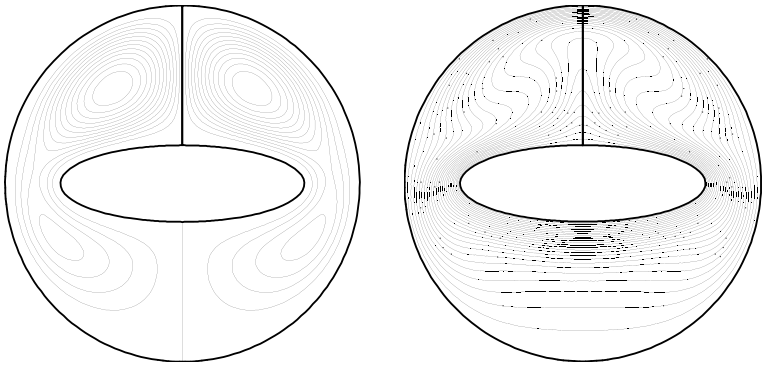

Fig. 3. Typical streamlines and isotherms for "O–H" configuration ($Ra = 10^4$, $Pr = 0.71$, $rr = 2.6$, $\varepsilon_o = 0$, $\varepsilon_i = 0.95$).

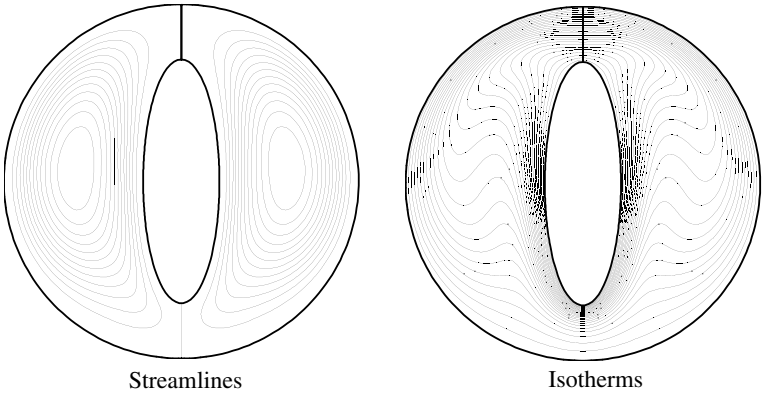

Fig. 4. Typical streamlines and isotherms for "O–V" configuration ($Ra = 10^4$, $Pr = 0.71$, $rr = 2.6$, $\varepsilon_o = 0$, $\varepsilon_i = 0.95$).

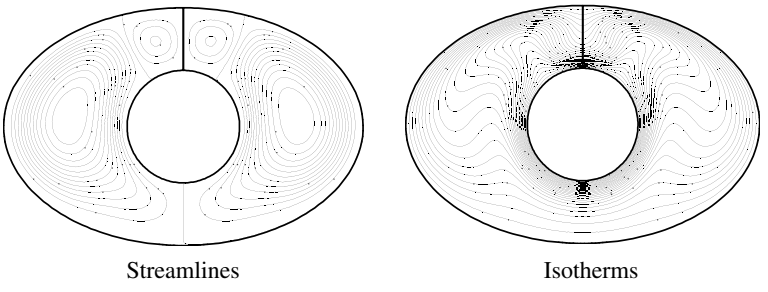

Fig. 5. Typical streamlines and isotherms for "H–O" configuration ($Ra = 10^4$, $Pr = 0.71$, $rr = 2.6$, $\varepsilon_o = 0.75$, $\varepsilon_i = 0$).

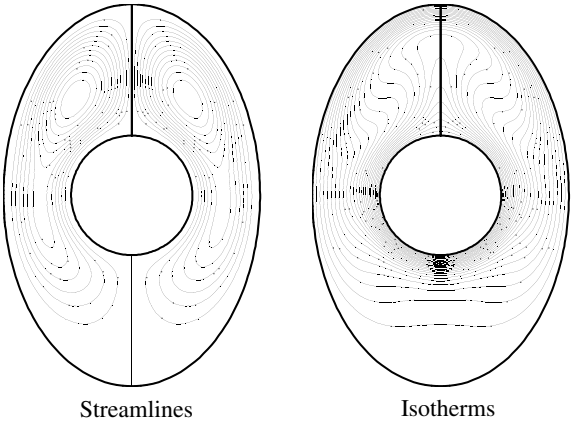

Fig. 6. Typical streamlines and isotherms for "V–O" configuration ($Ra = 10^4$, $Pr = 0.71$, $rr = 2.6$, $\varepsilon_o = 0.75$, $\varepsilon_i = 0$).

the eccentricity. The typical streamlines and isotherms for the case of $\varepsilon_o = 0.75$, $\varepsilon_i = 0$ are shown in Fig. 5, where four vortices and three plumes can be seen clearly.

For the "V–O" configuration, the flow and thermal patterns change very little. There is a pair of vortices. When ε_o increases, the two vortices shift up gradually. When ε_o increases from 0.25 to 0.50, the two vortices shift up to certain positions. As a result, the space between the two cylinders along the horizontal axis reduces, and the maximum stream function value reduces from 12.88 to 12.56. When ε_o further increases to 0.75, the two vortices shift to the locations above the inner cylinder, where the vertical gap is increased. This helps to increase the strength of the stream function in the space between the two cylinders and leads to the increase of the maximum stream function value from 12.56 to 13.48, as shown in Table 3. One plume exists for this case. The average Nusselt number keeps little change for $\varepsilon_o = 0.25$ and 0.50, but reduces slightly from 3.34 to 3.30 when ε_o increases from 0.50 to 0.75. The typical streamlines and isotherms for the case of $\varepsilon_o = 0.75$, $\varepsilon_i = 0$ are shown in Fig. 6, where two vortices and one plume can be seen clearly.

As shown in Table 4, for the "H–H" configuration, there are 16 cases studied in this work. When $\varepsilon_o = 0.25$, 0.5, and ε_i increases from 0.25 to 0.95, the flow and thermal patterns are similar to the case of "O–H" configuration. However, when ε_o is fixed at 0.75, and ε_i is increased from 0.25 to 0.95, the flow and thermal patterns are different from the case of "O–H" configuration. With $\varepsilon_i = 0.25$ and 0.50, there are four vortices instead of two developed above the inner cylinder, and two plumes plus

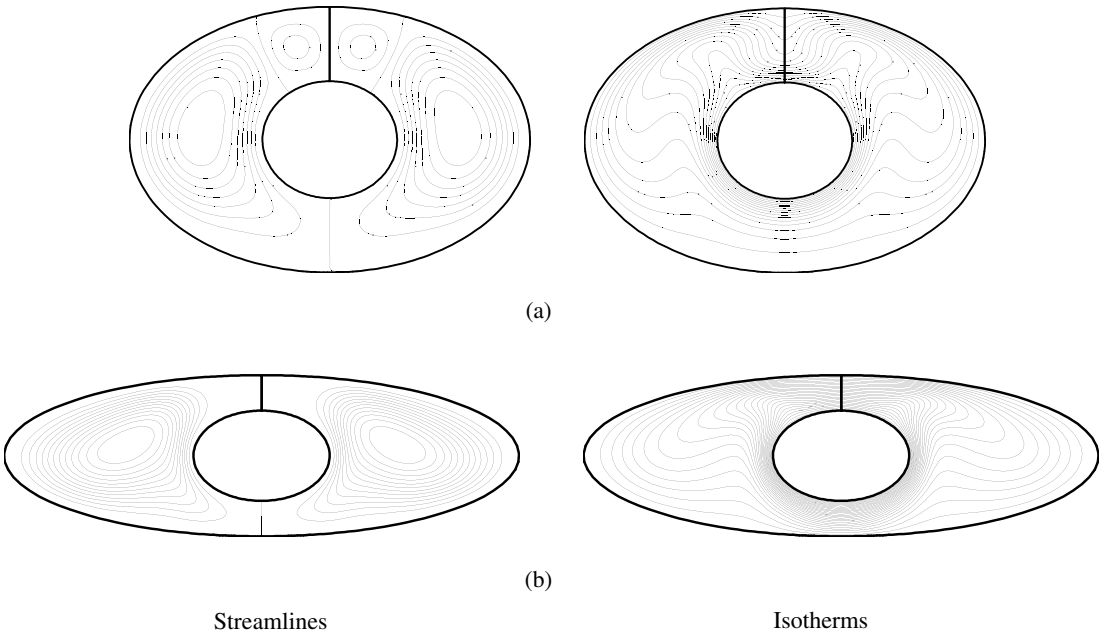

Fig. 7. Typical streamlines and isotherms for "H–H" configuration ($Ra = 10^4$, $Pr = 0.71$, $rr = 2.6$): (a) $\varepsilon_o = 0.75$, $\varepsilon_i = 0.50$, (b) $\varepsilon_o = 0.95$, $\varepsilon_i = 0.75$.

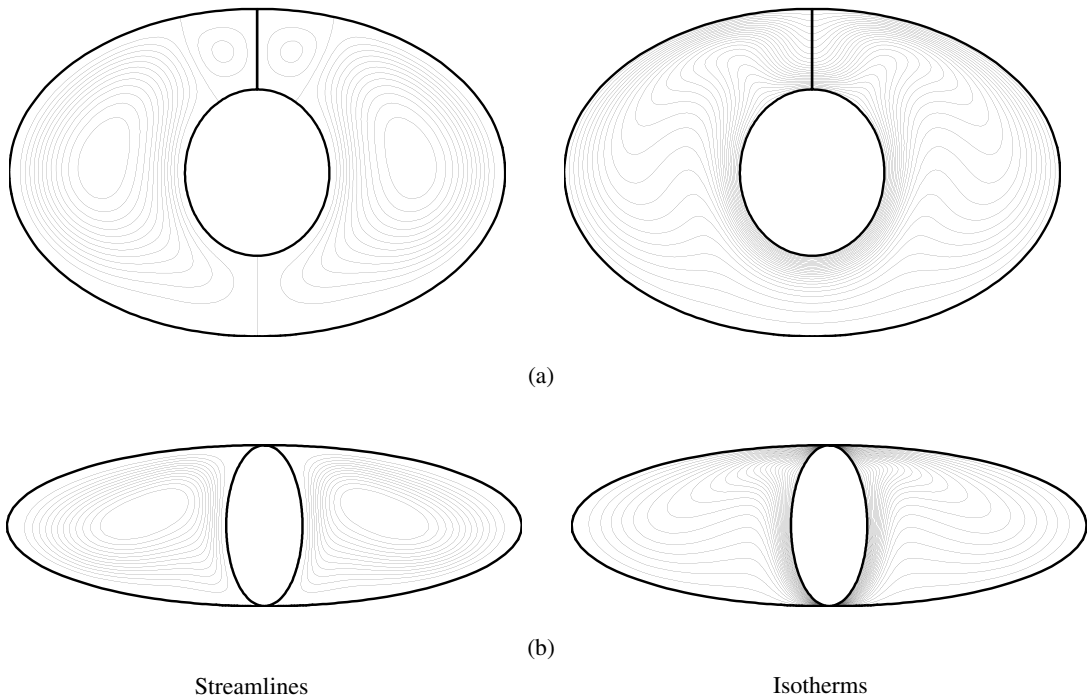

Fig. 8. Typical streamlines and isotherms for "H–V" configuration ($Ra = 10^4$, $Pr = 0.71$, $rr = 2.6$): (a) $\varepsilon_o = 0.75$, $\varepsilon_i = 0.50$, (b) $\varepsilon_o = 0.95$, $\varepsilon_i = 0.88$.

one additional plume in the inverse direction appear in the isotherms. The additional plume produces an additional narrow thermal boundary layer at the top of the inner cylinder and thus increases $\overline{Nu}$. As discussed above,

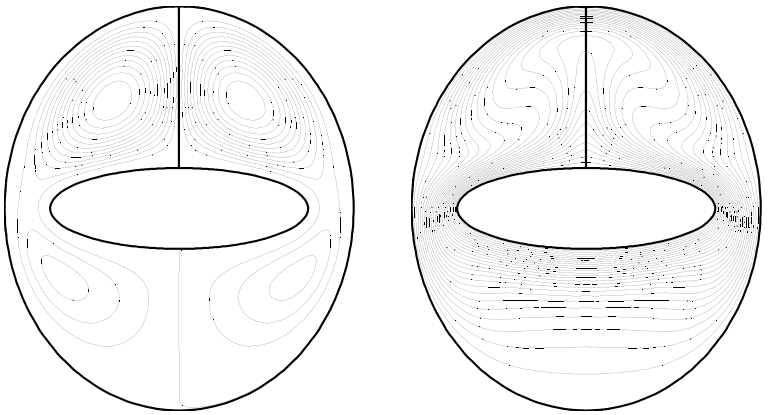

Fig. 9. Typical streamlines and isotherms for "V–H" configuration ($Ra = 10^4$, $Pr = 0.71$, $rr = 2.6$, $\varepsilon_o = 0.50$, $\varepsilon_i = 0.95$).

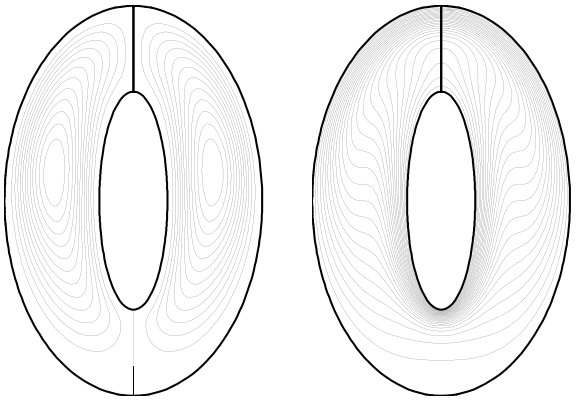

Fig. 10. Typical streamlines and isotherms for "V–V" configuration ($Ra = 10^4$, $Pr = 0.71$, $rr = 2.6$, $\varepsilon_o = 0.75$, $\varepsilon_i = 0.95$).

the two additional vortices are developed probably due to the appropriate space above the inner cylinder in the physical domain. The two additional vortices located above the inner cylinder reduce the strength of the flow and lead to the smaller maximum stream function value. The above flow and thermal patterns can be observed in Fig. 7(a) for the case of $\varepsilon_o = 0.75$, $\varepsilon_i = 0.5$. When ε_i is further increased, the inner cylinder becomes wider and wider, which forces the primary flow to move upward and downward. As a result, the top two vortices will gradually disappear. So, at $\varepsilon_i = 0.75$ and 0.95, there are only two vortices located beside the inner cylinder, and only one plume appears in the isotherms. When ε_o is fixed at 0.95, and ε_i is increased from 0.25 to 0.95, the flow and thermal patterns change very little, which are shown in Fig. 7(b) for the case of $\varepsilon_o = 0.95$, $\varepsilon_i = 0.75$. There is a pair of vortices located beside the inner cylinder, and two plumes appear above the inner cylinder.

For the "H–V" configuration, there are 16 cases studied in this work. The maximum stream function values and average Nusselt numbers of these cases are shown in Table 5. Like the "H–H" configuration, when $\varepsilon_o = 0.25$, 0.5, and ε_i increases from 0.25 to 0.95, the flow and thermal patterns are similar to the case of "O–V" configuration. When ε_o is taken as 0.75, and ε_i is increased from 0.25 to 0.75, the flow and thermal patterns are different from the cases of $\varepsilon_o = 0.25$, 0.5. There are four vortices above the inner cylinder, and the strength of the stream function value reduces with the increases of ε_i. Accordingly, two plumes plus one plume in a reverse direction occur above the inner cylinder. The $\overline{Nu}$ decreases gradually from 3.49 to 3.31 when ε_i increases from 0.25 to 0.75, since the thin boundary layer at the top of the inner cylinder produced by the additional plume in a reverse direction gets weaker and weaker. It then increases to 3.46 at $\varepsilon_i = 0.95$, where the ends of the major axes of the inner cylinder is very close to the outer boundary, and conduction takes more effect, leading to the increase of $\overline{Nu}$. The typical flow and thermal patterns of this case can be seen from Fig. 8(a) where $\varepsilon_o = 0.75$, $\varepsilon_i = 0.5$. When ε_o is fixed at 0.95, the outer cylinder becomes very wider and the eccentricity of the inner cylinder becomes less effective. The ψ_{max} keeps little change for all the eccentricities of the inner elliptic cylinder. The $\overline{Nu}$ increases gradually from 3.80 to 4.55 when ε_i increases from 0.25 to 0.75, while it increases from 4.55 to 34.41 when ε_i increases from 0.75 to 0.88. The increase is much larger when ε_i changes from 0.75 to 0.88 than that when ε_i changes from 0.25 to 0.75, since at $\varepsilon_i = 0.88$, the ends of the inner cylinder are very close to the outer cylinder and conduction takes more effect. At $\varepsilon_i = 0.88$, the end of the inner cylinder almost touches the outer cylinder and $\overline{Nu}$ increases greatly. The flow and thermal patterns for the case of $\varepsilon_o = 0.95$, $\varepsilon_i = 0.88$ are shown in Fig. 8(b). It is indicated that we failed to get

converged results for the case of $\varepsilon_o = 0.95$, $\varepsilon_i = 0.95$ because the ends of the inner cylinder touch the outer cylinder for this case.

For the "V–H" configuration, the flow and thermal patterns are similar to the case of "O–H" configuration. The maximum stream function values and average Nusselt numbers of this configuration are given in Table 6, and the typical streamlines and isotherms for the case of $\varepsilon_o = 0.50$, $\varepsilon_i = 0.95$ are shown in Fig. 9, which is similar to Fig. 3.

For the "V–V" configuration, the flow and thermal patterns are similar to the case of "O–V" configuration. The maximum stream function values and average Nusselt numbers of this configuration are displayed in Table 6, and the typical streamlines and isotherms for the case of $\varepsilon_o = 0.75$, $\varepsilon_i = 0.95$ are shown in Fig. 10, which is similar to Fig. 4.

8. Conclusions

In this paper, natural convection in horizontal annuli between two elliptic cylinders is numerically studied. The DQ method is employed to discretize the derivatives in the governing equations and boundary conditions.

The computational results are compared with available data in the literature and good agreement has been achieved. A sum of 68 different physical domains has been considered. A systematic study is conducted for the analysis of flow and thermal fields at different eccentricities of inner and outer elliptic cylinders. It was found that the position of the major axis of the inner elliptic cylinder takes effect on the streamlines, and very little effect on the average Nusselt number. When the major axis of the inner elliptic cylinder is in a vertical position, the maximum stream function value is increased, and in general, the average Nusselt number is slightly higher that that in a horizontal position. For the streamlines and isotherms, when the major axis of the outer cylinder is placed horizontally, at an appropriate space above the inner cylinder, two additional vortices in the streamlines and three plumes in the isotherms may occur and such phenomena need further investigation.

Acknowledgements

The second author acknowledges the support of Hitachi Scholarship Foundation for his visit to Institute of Fluid Science, Tohoku University, for the above work.

References

[1] T.H. Kuehn, R.J. Goldstein, An experimental and theoretical study of natural convection in the annulus between horizontal concentric cylinders, J. Fluid Mech. 74 (1976) 695–719.
[2] T.H. Kuehn, R.J. Goldstein, An experimental study of natural convection heat transfer in concentric and eccentric horizontal cylindrical annuli, J. Heat Transfer 100 (1978) 635–640.
[3] G. Guj, F. Stella, Natural convection in horizontal eccentric annuli: numerical study, Numer. Heat Transfer A 27 (1995) 89–105.
[4] J.H. Lee, T.S. Lee, Natural convection in the annuli between horizontal confocal elliptic cylinders, Int. J. Heat Mass Transfer 24 (1981) 1739–1742.
[5] W.C. Schreiber, S.N. Singh, Natural convection between confocal horizontal elliptical cylinders, Int. J. Heat Transfer 28 (1985) 807–822.
[6] C.H. Cheng, C.C. Chao, Numerical prediction of the buoyancy-driven flow in the annulus between horizontal eccentric elliptical cylinders, Numer. Heat Transfer A 30 (1996) 283–303.
[7] M.M. Elshamy, M.N. Ozisik, J.P. Coulter, Correlation for laminar natural convection between confocal horizontal elliptical cylinders, Numer. Heat Transfer A 18 (1990) 95–112.
[8] F. Stella, G. Guj, Vorticity–velocity formulation in the computation of flows in multiconnected domains, Int. J. Numer. Meth. Fluids 9 (1989) 1285–1298.
[9] R.E. Bellman, B.G. Kashef, J. Casti, Differential quadrature: a technique for the rapid solution of nonlinear partial differential equations, J. Comput. Phys. 10 (1972) 40–52.
[10] C. Shu, Differential Quadrature and its Application in Engineering, Springer-Verlag, London, 2000.
[11] C. Shu, B.E. Richards, Application of generalized differential quadrature to solve two-dimension incompressible Navier–Stokes equations, Int. J. Numer. Meth. Fluids 15 (1992) 791–798.
[12] C. Shu, H. Xue, Solution of Helmholtz equation by differential quadrature method, Comput. Meth. Appl. Mech. Eng. 175 (1999) 203–212.
[13] C.W. Bert, M. Malik, Differential quadrature method in computational mechanics: a review, Appl. Mech. Rev. 49 (1996) 1–28.
[14] H. Du, M.K. Lim, R.M., Application of generalized differential quadrature method to structural problems, Int. J. Numer. Meth. Eng. 37 (1994) 1881–1896.
[15] C. Shu, K.S. Yeo, Q. Yao, On the performance of three iterative methods for the solution of GDQ algebraic equations, Comp. Meth. Appl. Mech. Eng. 167 (1998) 1–15.
[16] C. Shu, Q. Yao, K.S. Yeo, Y.D. Zhu, Numerical analysis of flow and thermal fields in arbitrary eccentric annulus by differential quadrature method, Heat Mass Transfer 38 (2002) 597–608.